Chaos, Solitons and Fractals 198 (2025) 116586

Contents lists available at ScienceDirect

Chaos, Solitons and Fractals

journal homepage: www.elsevier.com/locate/chaos

Electric-field-biased control of irregular oscillations via multistability in a nonlinear terahertz meta-atom

Gervais Dolvis Leutcho *, Gabriel Gandubert, Lyne Woodward, François Blanchard

Département de Génie Électrique, École de technologie supérieure (ÉTS), Montréal, Québec H3C 1K3, Canada

ARTICLE INFO

Keywords:
Nonlinear meta-atom
EM radiation
Bifurcation
Regular and irregular signals

ABSTRACT

The split-ring resonator (SRR) has become widely popular in the design of artificial two-dimensional materials at the sub-wavelength scale, known as metasurfaces. When exposed to an intense electric field, this meta-atom deposited on a suitable substrate can exhibit electromagnetic coupling and become a bianisotropic meta-atom metasurface, where various nonlinear phenomena can occur. In this paper, the collective properties of the nonlinear SRR meta-atom model subjected to an alternating current (AC) and direct current (DC) field in the terahertz (THz) frequency portion of the spectrum are investigated in detail. Our investigation seeks to identify a new pathway to leverage the controlled bias field for reducing the required AC field that triggers the desired nonlinear effects. Using bi-parameter diagrams, we demonstrate how irregular oscillations emerge from controlling the DC field with a relatively low AC field. This result represents a key strategy and a promising route for translating these significant nonlinear interactions into practical, real-world applications utilizing nonlinear metasurfaces. To further examine some interesting properties correlated to the multi-sensitivity of the material in the low AC field regime, we first consider the normalized amplitude of the AC field as a control parameter for a fixed DC value. This approach reveals important phenomena, such as the transition to chaos via period-splitting bifurcation, as well as the emergence of multistable windows where the system exhibits a variety of coexisting periodic signals, including the coexistence of two and three distinct periodic patterns. Additionally, we uncover a rare case of bistability consisting of two different irregular signals. Next, the dynamic characteristics of the system are analyzed by varying the normalized DC field, for a fixed value of the normalized AC amplitude. In this situation, an interesting route to chaos is found through the creation and annihilation of periodic orbits. We also highlight a striking region in which the system exhibits the coexistence of three or two regular and irregular behaviors, resulting from a combination of hysteresis and parallel bifurcations. To distinguish these coexisting patterns, we compute the cross-sections of the initial domain, phase images, and time series associated with each signal. These findings substantially advance the development of multifunctional metasurface-based devices, with potential applications ranging from secure communication systems to enhanced signal detection.

1. Introduction

The electromagnetic (EM) frequency range between 300 GHz and 10 THz, known as the "THz gap", lies between electronics and photonics. It has long had limitations in terms of signal generation, guidance, processing and control. Today, however, it is attracting growing interest and showing increasing promise in a wide range of fields and applications [1]. Over the past decade, the field of terahertz (THz) wave research has expanded to include the study and potential manufacture of nonlinear optical devices and materials [2–7]. This recent expansion of THz science towards nonlinear interactions has been fueled by the development of intense THz sources [8–10], which are essential to enable nonlinear behavior in this frequency range [11]. This is particularly interesting with devices based on nonlinear metamaterials (MM) and/or metasurfaces (MS), which have recently emerged as powerful tools for exploring and unlocking the potential of this new regime [2,4–6]. Although traditionally used in the design of microwave devices, nonlinear metamaterials are now being extended to the THz range. Consequently, nonlinear MM engineering is one of the promising avenues for research and development of new nonlinear photonic devices, meta-electronic devices [12,13] and materials operating at THz frequency.

* Corresponding author.
E-mail addresses: leutchoeinstein@yahoo.com (G.D. Leutcho), lyne.woodward@etsmtl.ca (L. Woodward), francois.blanchard@etsmtl.ca (F. Blanchard).

https://doi.org/10.1016/j.chaos.2025.116586
Received 14 March 2025; Received in revised form 15 April 2025; Accepted 12 May 2025
Available online 19 May 2025

Metasurfaces are two-dimensional (2D) structures of metamaterials that exhibit extraordinary properties when exposed to incident radiation [5,14]. Indeed, they are artificially engineered on a scale well below the wavelength, so that the response to an EM wave is precisely dictated/controlled by the microstructure. The best-known metamaterials are those with negative refractive indices (i.e., both permeability and permittivity are negative), which can be designed using split-ring resonators (SRRs) as meta-atoms [15]. Therefore, much attention has been paid to the design of metasurfaces based on SRRs due to their unique and interesting interaction with EM waves [14,15]. In fact, the SRR is a well-known unit cell that promotes charge accumulation due to its gap, which acts as a barrier to the flow of circulating current [5,16]. Following the application of an intense electric field by intense incident radiation on the surface of the structure deposited on a suitable substrate, the motion of charge carriers in the gap junction can induce complex nonlinear effects including regular and irregular oscillations, bifurcation, hysteresis, to name a few [17,18]. Interestingly, these nonlinear effects can lead to phenomena such as multistability and various transition paths, including period-doubling and period-bubbling. Multistability, where multiple stable states coexist, has been studied in several dynamical systems, including nanoparticle food chain models [19], predator-prey interactions [20], and nonlinear acoustic-gravity waves in a rotating atmosphere [21]. In the context of period-doubling and period-bubbling, these pathways are critical for explaining the transition to chaotic behavior, as explored in several studies [22,23]. These concepts are essential for understanding the nonlinear dynamics in systems exposed to intense EM radiation, as described in this paper. In this context, a coupled nonlinear U-shaped split-ring resonator has been considered and investigated [24]. Taking into account the magnetic coupling between the two SRRs, its model has been derived to study its nonlinear properties. The one-dimensional bifurcation diagram was used to show the region where regular and irregular oscillations can be observed when the normalized drive frequency is varied. Next, by considering two structures of the same meta-atom-based SQUIDs (for superconducting interference devices) coupled by their mutual inductance, their dynamic behavior has been studied numerically when the model is driven by a harmonic field [25]. The authors demonstrated that the proposed coupled SQUID material is capable of exhibiting multi-branch resonance, a quasi-periodic transition to chaos, and hysteretic resonance. Using the bifurcation and Lyapunov exponent analysis, the nonlinear behavior of the RLD (resistor–inductor–diode) circuit was predicted with a nonlinearity resulting from the parallel combination of a semiconductor rectifier diode and a fixed capacitor [26]. In [27], the authors generate and control chimera states in the SQUID metasurface when the model is biased by a time-independent (DC) flux gradient and driven by a sinusoidal (AC) flux field. The appearance of chimera states in the introduced ring metasurface, interrupted by a Josephson nonlinearity was monitored by adjusting the DC flux or the AC field amplitude. It is important to emphasize that all the above work has been studied in the frequency range of a few GHz (gigahertz), which is a limit for certain applications (e.g., telecommunications, imaging, sensing, etc.) [28]. For the THz range, due to the need for intense sources to induce these nonlinearities, this approach remains largely limited to research laboratories. Fortunately, it has been demonstrated in various contexts that applying a DC electric field could be a key solution to facilitate the desired interactions, such as nonlinear interactions [12,29]. To date, however, electric-field-biased control of birth of irregular oscillations via multistability in a nonlinear THz meta-atom hasn't been investigated numerically and remains an open problem.

This paper presents the charge carrier dynamics of the generalized U-shaped nonlinear SRR model in the THz frequency portion. The main contributions and novelty of this work are summarized as follows.

i) Investigates the onset of irregular oscillations under a low AC field, with the DC field as the controlling factor. Using bi-parameter diagrams, the study examines how the DC field triggers the emergence of nonlinear behavior at low AC fields, which is the core contribution of this research.
ii) The transition between different oscillation modes is studied using bifurcation diagrams and the maximum Lyapunov exponent (MLE). The results indicate two important scenarios leading to irregular oscillations: (a) a period doubling transition and (b) a transition involving the formation and destruction of bifurcation bubbles (also known as period-bubbling).
iii) We have numerically explored the parameter-relied bifurcations, revealed the interesting phenomenon of coexisting bifurcations and attractors, and comprehensively described its mechanisms.
iv) By analyzing the parallel branch and the enlargement of the hysteresis zones, we have detected a region of periodic tristability and a large zone where two MLE are all positive, characterizing the existence of one of the rare chaotic bistability. To the best of the authors' knowledge, such a striking bistability and tristability have not been reported in the literature on such a material and thus deserve dissimilation.

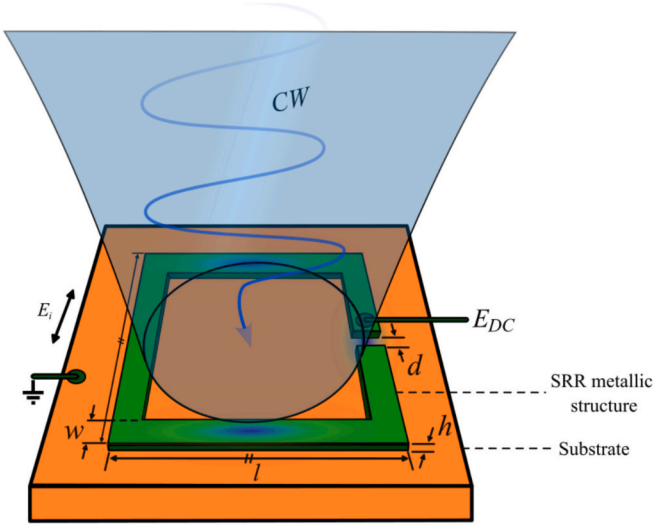

Fig. 1. The physical structure of the bianisotropic meta-atom metasurface is illuminated by a continuous wave (*CW*) and controlled by a constant polarization field (E_{DC}).

The paper is organized as follows. In Sec. 2, we derive and present the physical model describing the dynamics of the carriers in the gap of the meta-atom. The collective nonlinear behavior of the meta-atom metasurface is well studied and discussed in Sec. 3. We summarize this work with a conclusion in Sec. 4.

2. The physical model and its description

The sketch of the SRR material under study is shown in Fig. 1. It consists of a single-gap square-shape meta-atom of thickness h, length l, line width w. The material is illuminated with an electromagnetic wave of a specific polarization. E_i is the electric field and the double arrow indicates its polarization. It is also subjected to a DC bias voltage (i.e., time-invariant component), E_{DC}, which can be useful to control the surface loss and thus enhance the field in the gap. The incidence EM radiation induced a circulating current in the ring which promotes charge storage in the gap. The gap of width d thus behaves as a nonlinear capacitor (due to the intense field) whose voltage dependence is expressed in [30]. The ring (metal frame) forms the material coil (with self-inductance L and ohmic resistance R). Recently, the physical modeling of the material has made it possible to extract the total charge Q_{jn} accumulated inside the gap and to establish its mathematical model when illuminated by an electromagnetic wave [17]. In order to generate

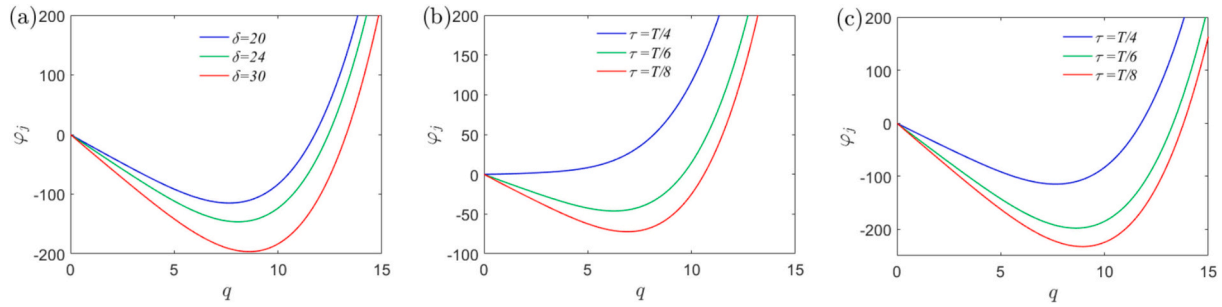

Fig. 2. Curve of the normalized potential φ_j expressed in Eq. (5) for $\beta = 0.4$, $\eta = 0.08$. (a) for $\mu = 0$, (b) $\delta = 0$ and $\mu = 20$, (c) $\delta = 20$ and $\mu = 20$.

a complex nonlinear response with a weaker field, we have proposed an improved model given by Eq. (1), in which a DC field is added to the AC field.

$$L\frac{dI}{dt} + RI + \left[\frac{Q_{jn}}{C_{0j}V_\xi} - \frac{\gamma}{2}\frac{Q_{jn}^2}{C_{0j}^2V_\xi^2} + \frac{\gamma(2\gamma-1)}{6}\frac{Q_{jn}^3}{C_{0j}^3V_\xi^3}\right]V_\xi = E_{DC} + E_{ind}(t) \tag{1}$$

where I is the current flowing in the ring, V_ξ is the intrinsic potential, C_{0j} is the zero-bias junction capacitance, d/dt is the first derivative with respect to time t, γ is the gradient coefficient, and E_{DC} is the applied DC field. The electromotive force $E_{ind}(t)$ induced by the incident radiation is given by

$$E_{ind}(t) = \int E_i \bullet dl = E_0 cos(\Omega t) \tag{2}$$

where E_i is the electric field, E_0 and Ω are the amplitude and driving frequency of the field, respectively. The following transformation of variables and parameters are established and used to normalize eq. (1) in the adimensional space (τ, q):

$$\begin{cases} I = \dfrac{C_{0j}V_\xi}{\sqrt{LC_{0j}}}\dfrac{dq}{d\tau}, t = \tau\sqrt{LC_{0j}}, Q_c = C_{0j}V_\xi, \Omega = \omega \Big/ \sqrt{LC_{0j}} \\ \sigma = R\sqrt{\dfrac{C_{0j}}{L}}, \mu = \dfrac{E_0C_{0j}}{Q_c}, \beta = \dfrac{\gamma Q_c}{2V_\xi C_{0j}}, \eta = \dfrac{\gamma(2\gamma-1)Q_c^2}{6V_\xi^2C_{0j}^2}, \delta = \dfrac{E_{dc}}{V_\xi}. \\ q = \dfrac{Q_{jn}}{C_{0j}V_\xi} \end{cases} \tag{3}$$

Here, σ stands for the normalized loss parameter, μ and ω are the normalized amplitude and frequency of the AC field, respectively. δ is the bias term derived from the applied DC field, while β and η are the nonlinearity parameters. Substituting Eq. (3) into Eq. (1), we derive the nonlinear model describing the dynamics of the normalized current (i) flow in the ring and the normalized charges (q) accumulated in the gap of the bianisotropic meta-atom metasurface subjected to both AC and DC fields as given in Eq. (4).

$$\begin{cases} \dot{q} = i, \\ \ddot{q} + \sigma\dot{q} = -\dfrac{d\varphi_j}{dq}, \end{cases} \tag{4}$$

where the dot indicates the derivative with respect to the normalized time τ, and the normalized potential φ_j is expressed by

$$\varphi_j(q,\tau) = \frac{1}{2}q^2 - \frac{\beta}{3}q^3 + \frac{\eta}{4}q^4 - (\delta + \mu cos(\omega\tau))q. \tag{5}$$

Without electric field illumination of the meta-atom surface (i.e., $\mu = 0$), the normalized potential φ_j depends on the normalized charge in the gap and the bias term δ and is time independent. In this case, the polarization of the gap junction is varied by adjusting the DC field values. When the material is now illuminated with an incident harmonic field (i.e., $\mu \neq 0$), the potential becomes time-dependent. In addition to varying with time, it can also fluctuate as a function of the applied DC field, inducing highly exciting and complex dynamics. Fig. 2(a)-(c) illustrates each of the above scenarios and depicts how the shape of the potential varies with DC field [Fig. 2(a)], AC field [Fig. 2(b)], or both fields [Fig. 2(c)]. The last two cases show the evolution in the time interval $\tau \in]0, T/4]$, where $T = 2\pi/\omega$ is the normalized period. This work deals with the latter case, using bifurcation diagrams with their corresponding Lyapunov exponents, the power spectrum to demonstrate the emergence of attractors, and the basin of attraction with phase images to characterize the coexistence of different attractors. The fundamental oscillation frequency of the system f (obtained in the lossless, entrainment-free case) strongly depends on the geometric parameters of the SRR material and can be described by the formula

$$f = \left(\frac{c_0}{2\pi l\sqrt{\varepsilon_r}}\right)\sqrt{\frac{d}{w}} = \frac{\omega_0}{2\pi} \tag{6}$$

where $c_0 = 3 \times 10^8\, m.s^{-1}$ is the speed of light in vacuum, ε_r is the relative permittivity of the medium, ω_0 is related to the physical parameters by $\omega_0 = 1/\sqrt{LC_{0j}}$, with $L = \mu_0 l^2/h$ and $C_{0j} = \varepsilon wh/d$. μ_0 represents the permeability of free space and ε is the permittivity of the medium between the armatures (i.e., the response of the medium to an electric field). The meta-atom metasurface in Fig. 1 is designed with the geometric parameters $w = 6\mu m$, $h = 300nm$, $d = 4\mu m$, and $l = 60\mu m$ for an oscillation frequency of $f = 0.4THz$. These parameters are based on a real structure previously published in [3,31,32].

3. Collective nonlinear properties of the meta-atom

In this section, we present and discuss the results of the striking nonlinear properties of the meta-atom metasurface modeled by Eq. (4) in the THz frequency range. First, the birth of irregular oscillations at low alternating field is presented using bi-parameter diagrams. Under this condition, the window of multisensitivity and multistability in the parameter space is analyzed. Then, a graph of the maximum Lyapunov exponent is used to highlight a window of hysteresis revealed in the bi-parameter space. To obtain the dynamics in two-dimensional space, the Wolf algorithm [33] is used to numerically compute and analyze the maximum Lyapunov exponent (MLE) on a grid of 600 × 600 values of the defined space parameters. A fourth-order Runge-Kutta algorithm with a fixed step size of 0.002 is also used to integrate the model. In the fourth subsection, the bifurcation diagrams are used to explore the emergence of attractors in the system, and the exciting phenomenon of coexisting attractors is examined in detail. The last subsection presents the complete dynamical characteristics of the system when the bias term is considered as the only bifurcation parameter.

3.1. Birth of irregular oscillations at low alternating field

To demonstrate the birth of irregular oscillations at low AC field values in response to a high AC destruction scenario, we study the dynamics of the system in the two-dimensional space defined by the pa-

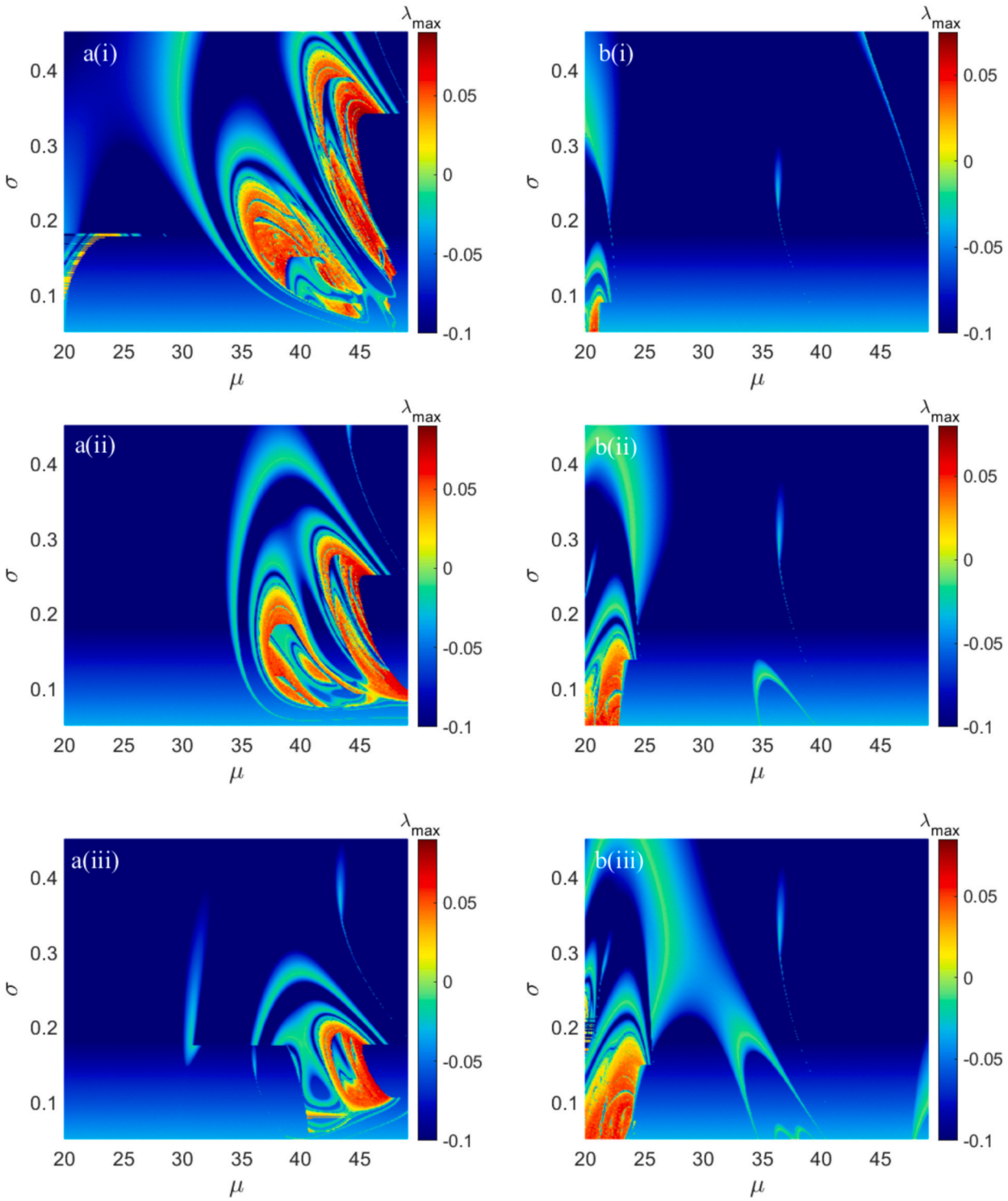

Fig. 3. Spatial diagrams in the $\mu - \sigma$ plane showing birth with the emergence of irregular oscillations (area in the color bar where $\lambda_{max} > 0$) in the range of high (a) and low (b) values of the normalized AC field for different values of the normalized DC field δ. The initial points used are $q_0 = 0.3, i_0 = 0.1$ and the other parameters are set to $\omega = 1.0$, $\beta = 0.4$, and $\eta = 0.08$. From a(i) to a(iii), $\delta = (5, 9, 12)$ and from b(i) to b(iii), $\delta = (15, 17, 18)$.

rameters μ and σ. This analysis is carried out by gradually monitoring the normalized bias constant δ. For this purpose, the following dynamic range was considered: $20 \leq \mu \leq 49$ for the normalized AC field amplitude parameter, and $0.05 \leq \sigma \leq 0.45$ for the normalized loss parameter. To construct the bi-parameter diagrams in the (μ, σ) space, we vary the two control parameters μ and σ, starting from $\mu_{min} = 20$ and $\sigma_{min} = 0.05$ up to $\mu_{max} = 49$ and $\sigma_{max} = 0.45$, with initial values ($q_0 = 0.3$, $i_0 = 0.1$), while keeping the other parameters fixed at $\omega = 1.0$, $\beta = 0.4$, $\eta = 0.08$. For each pair of parameters, the values of the maximum Lyapunov exponent (MLE) are then analyzed. When we smoothly adjust the normalized DC field parameter, different dynamics are observed that better explain the death of irregular oscillations at high AC field values or their birth at relatively low alternating field values. First, for normalized DC field values $\delta = 5$ and $\delta = 9$, two distinct bands of irregular oscillations appear in the two-parameter space, as shown in Fig. 3a(i) and a(ii), respectively. For $\delta = 12$, a single band of irregular

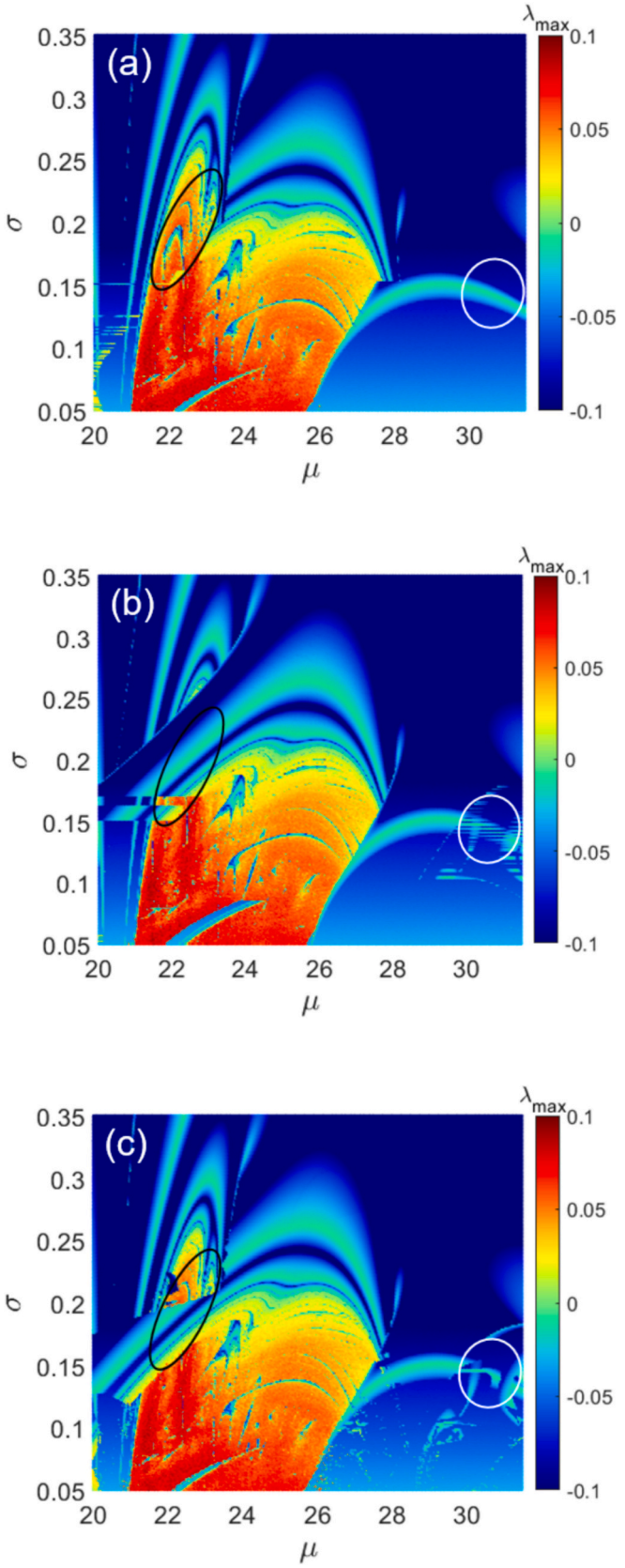

(caption on next column)

Fig. 4. Space diagrams in the $\mu - \sigma$ plane for two different initial points (q_0, i_0), showing the regular, irregular and hysteresis behaviors (circled areas) in the system. The space diagrams (a) and (c) are calculated by up-sweeping the normalized amplitude μ and loss parameter σ while (b) is calculated by down-sweeping these parameters. The color codes other than red indicate regular period nT oscillations and chaos is presented in red. The black and white circles denote regions of hysteresis dynamics (see text for more details). The initial points used are $q_0 = 0.3, i_0 = 0.1$ for (a) and (b); $q_0 = -4, i_0 = \sigma$ for (c). The other parameters are set to $\omega = 1.0$, $\beta = 0.4$, $\eta = 0.08$ and $\delta = 20$. (For interpretation of the references to color in this figure legend, the reader is referred to the web version of this article.)

oscillations is seen in parameter space, as shown in Fig. 3a(iii). These irregular behaviors emerge from three different critical values of μ, i.e., $\mu > 34.7$ for $\delta = 5$ [Fig. 3a(i)], $\mu > 36.5$ for $\delta = 9$ [Fig. 3a(ii)], and $\mu > 40$ for $\delta = 12$ [Fig. 3a(iii)]. In other words, irregular oscillations are mainly concentrated in the areas where the normalized AC field is high. This sequence demonstrates the death of irregular oscillations at high normalized AC field values as the normalized DC field values increase. This is even highlighted in Fig. 3a(ii) and a(iii), where it is clearly observed that the dynamic range of the irregular oscillations in parameter space shrinks as the normalized bias term δ increases. By further increasing the bias term δ, irregular oscillation modes then begin to be born in regions where the normalized AC field is low. Fig. 3b(i)-b (iii) show three situations illustrating these cases for $\delta = 15$, $\delta = 17$, and $\delta = 18$. In these last cases, we observe that there is no irregular oscillation in the region where $\mu > 25.5$. For example, when $\delta = 15$, irregular oscillations start to be born in a very small window of the two-parameter space and at low values of the normalized AC field, as shown in Fig. 3b (i). For $\delta = 17$, this irregular region expands, while remaining in the region of low values of the normalized AC field and not exceeding $\mu \approx 23.77$. As the bias term δ increases slightly further, this region expands again up to $\mu \approx 25.2$, as shown in Fig. 3b(ii). The exciting and interesting results presented in this subsection clearly show that there are critical values of the normalized DC parameter δ for which irregular oscillations can appear only at high values of the normalized AC parameter μ, as well as values of δ for which these oscillations can emerge only at low values of the normalized AC parameter. The latter case is of particular interest since it allows nonlinear effects to be induced and controlled at low AC fields simply by adjusting the DC parameter. Another interesting case is shown in Fig. 4, for a low AC field with $\delta = 20$. In this case, we have zoomed into the interval to demonstrate that the same scenario can occur via multistability (see section 3.2).

3.2. Analysis of multisensitive dynamic regions

In this subsection, we focus on the multisensitive dynamics in the low AC field region (as shown in Fig. 3(b)). In this case, we have shown that irregular oscillations emerge in the region $\mu < 28$, depending on the chosen value of the normalized DC bias constant δ. Therefore, to better explore the multisensitive dynamics, we consider the bi-parameter (μ, σ) space and analyze the zones between 20 and 31.5 for the value of μ and between 0.05 and 0.35 for the value of σ for $\delta = 20$. This striking multisensitivity (e.g., periodic oscillation, chaotic oscillation, multistable oscillations) of the nonlinear SRR material modeled by the nonlinear model (4) is obtained by analyzing the MLE when all other parameters are set to $\omega = 1.0$, $\beta = 0.4$, $\eta = 0.08$. The complex and rich dynamics of the system can be observed in the two-parameters phase diagrams shown in Fig. 4. The parameter range chosen in the $\mu - \sigma$ plane is the one featuring the most interesting dynamic characteristics. First, the system is numerically investigated when the value of the initial point is maintained at ($q_0 = 0.3$, $i_0 = 0.1$). In this case, the couple of parameters (μ, σ) is scanned upwards [Fig. 4(a)] and then downwards [Fig. 4(b)] in their corresponding regions ($20 \leq \mu \leq 31.5$ and $0.05 \leq \sigma \leq 0.35$). The MLE are recorded at each iteration until the pair

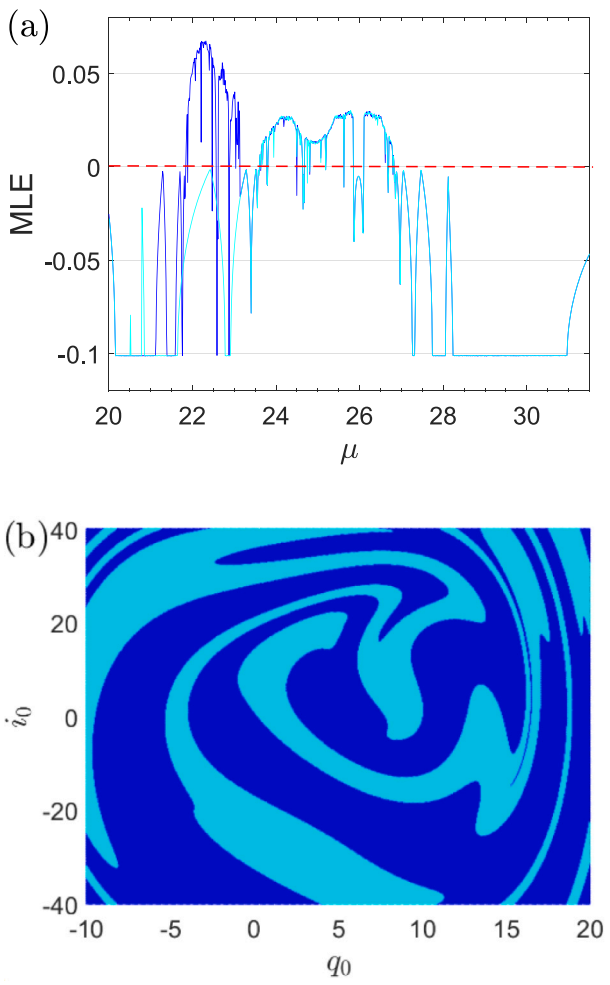

Fig. 5. (a) Maximum Lyapunov exponent for $\sigma = 0.2$ demonstrating three different dynamic regions (periodic, chaotic, or both chaotic and periodic) for decreasing (cyan) and increasing (blue) values of the normalized amplitude μ. (b) demarcation region (basin of attraction) of the coexistence of chaotic signal (blue) and periodic signal (cyan) obtained at $\mu = 22.43$. The rest of parameters are set as in Fig. 4. (For interpretation of the references to color in this figure legend, the reader is referred to the web version of this article.)

of parameters (μ, σ) attain their highest values $[\mu_{max} = 31.5, \sigma_{max} = 0.35]$. Next, we reinvestigate the dynamics of the system by scanning upwards the range of the pair (μ, σ) and updating the initial value of the normalized charge q_0 at each iteration according to $(q_0 = \sigma, i_0 = 0.1)$ and recording the MLE once more [Fig. 4(c)]. In other words, the initial value in this case changes at each iteration, anytime σ is updated. From the results reported in Fig. 4, we can now categorize the different dynamics exhibited by the nonlinear SRR model. Indeed, two main behaviors can be seen in Fig. 4 depending on the value of the maximum Lyapunov exponent indicated on the color bar segment. That is, an irregular behavior observed in red regions (where the MLE (λ_{max}) is positive) and a regular behavior observed in regions other than the red area (this case corresponds to negative values of the λ_{max}). We notice that irregular oscillations (i.e., chaotic behaviors) are predominant in the range $21 < \mu < 26.8$ and surrounded by two regular zones (i.e., $20 \leq \mu < 21$ and $26.8 \leq \mu \leq 31.5$). Also, some tiny windows of regular oscillations can be observed in the irregular domain of Fig. 4. By observing Fig. 4(a) and (c) and according to the values of λ_{max}, we can definitively conclude that the irregular oscillations are always localized in the region where $\sigma < 0.26$ and regular/periodic oscillations always in the region where $\sigma > 0.26$. Fig. 4(b) shows a slight shift in the bidimensional graph. Irregular oscillations are observed for $\sigma < 0.21$, whereas above this critical value, only regular oscillations can be found. This two-parameter projection is essential for detailed analysis and in-depth study of the different behaviors exhibited by the nonlinear SRR system. In addition to revealing areas of regular and irregular oscillations, various regions where coexisting patterns or multistability (places where each mark of difference is seen) is expected are also highlighted. By closely analyzing the graphs presented in Fig. 4, one can notice that they are not all identical. Differences can be appreciated, for example, by comparing Fig. 4(a)-(c) in the black and white circled areas. The coexisting dynamics observed are due, on one hand, to the shift observed in the irregular oscillation region in Fig. 4(b) and, on the other, to the hysteresis phenomenon uncovered in the system and highlighted by circled regions above when the control parameters are scanned up and down. We can therefore conclude that the proposed model exhibits the exciting phenomenon of multistability [24,34–37]. However, it is difficult to count both the number and the variety of coexisting patterns in the system with these two-parameter charts. In the coming sub-section, the maximum Lyapunov exponent and the basins of attraction will be exploited to investigate this particular feature of the model in detail and to determine the number of coexisting states that can emerge in each parameter range.

3.3. Coexisting graph of Lyapunov exponent

In this subsection, we explore the maximum Lyapunov exponent (MLE) and cross-section of the basins of attraction, to characterize the diverse nonlinear behaviors of the model and demonstrate the different types of signals that can coexist for a given parameter value. The normalized DC bias parameter δ used in the numerical computation is set as in Fig. 4 for $\sigma = 0.2$. The coexisting MLE shown in Fig. 5(a) enables to visualize and detect the regular periodic, irregular chaotic and hysteretic ranges when the normalize amplitude μ of the driving field is monitored. In this figure, the blue curve segment is obtained by sweeping upwards the normalized amplitude μ, while the cyan curve branch is generated by sweeping down the same parameter with the initial point $(q_0 = 0.3, i_0 = 0.1)$. From these overlaid graphs, the regular (periodic) and irregular (chaotic) regions can be well distinguished since the MLE is positive in chaotic regions (and negative in periodic regions). When the normalized amplitude μ is weak (i.e., when $\mu < \mu_{c1}$ where $\mu_{c1} = 21.8$), the nonlinear SRR exhibits the coexistence of periodic oscillation modes. In the hysteresis region defined by $\mu_{c1} \leq \mu \leq \mu_{c2}$ (where $\mu_{c2} = 23$), the MLE of the blue curve is positive while that of the cyan curve is negative. In this range, the nonlinear SRR model reveals the coexistence of an irregular mode (blue curve), where the value of the MLE does not breach 0.065, with a periodic mode (cyan curve). Besides, since the multistable region has a small width $(\Delta\mu = \mu_{c2} - \mu_{c1} = 1.2)$, a slight variation of the initial conditions is sufficient for the system to switch from one state to another. When the normalized amplitude μ exceeds the critical value $\mu_{c2} = 23$, the two maximal Lyapunov exponent branches merge, no hysteresis window is observed, and the system can only evolve in a chaotic or periodic mode. Compared to the irregular oscillation mode of the multistable region, the one of the monostable region is broader $(\Delta\mu = 3.2)$, however, the value of the MLE does not rise above 0.028. In Fig. 5(b), we plot the cross-section of the basin of attraction that allows the coexistence of the two modes (irregular and regular) demonstrated in the hysteresis region above for a value of the normalized amplitude $(\mu = 22.43)$. The cyan area corresponds to the domain of the pair of initial points (q_0, i_0) leading to a periodic signal, and the blue area is the domain of the initial points (q_0, i_0) converging towards a chaotic signal, as observed in Fig. 5(a).

3.4. Dynamic characteristic with normalized AC amplitude

The aim of this subsection is to investigate the different processes leading to irregular oscillations, the emergence of attractors, and the sensitivity of the system to a slight variation of the loss parameter (the

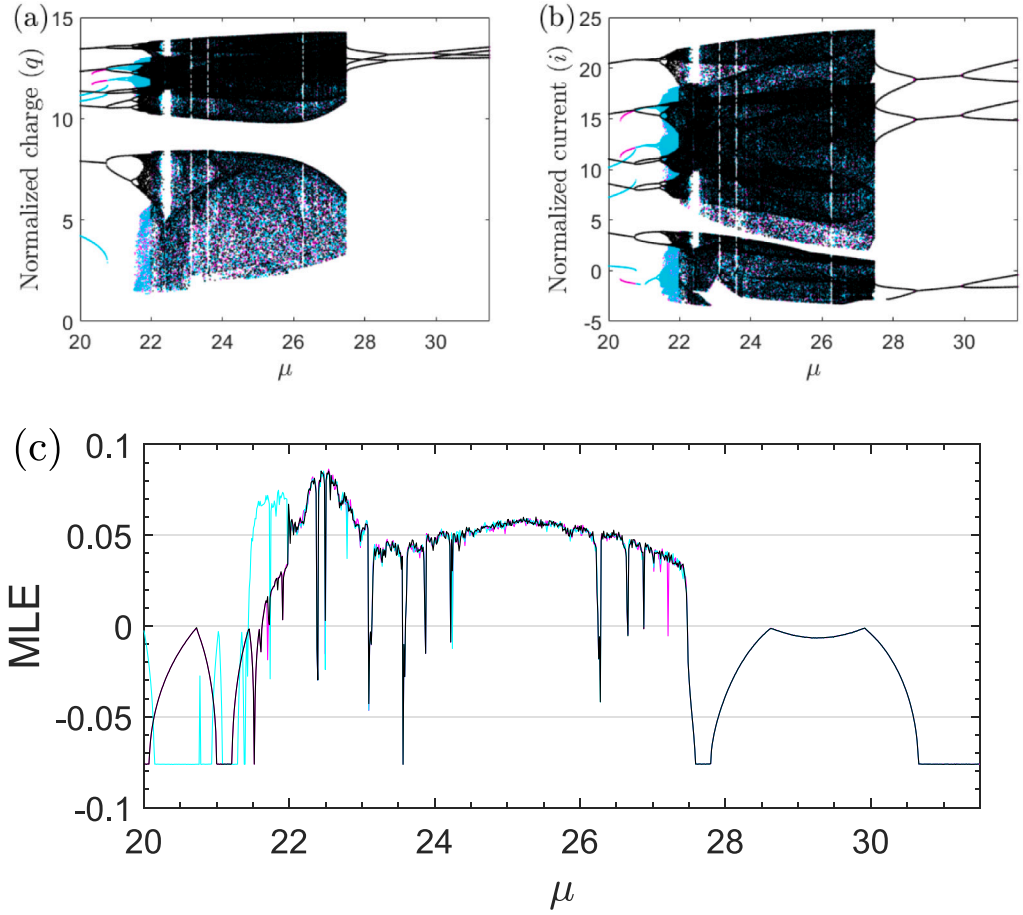

Fig. 6. (a)-(b) Bifurcation diagrams and corresponding maximum Lyapunov exponent (c) of the normalized charge and normalized current of the system for $\sigma = 0.15$. Scan up μ (cyan and black) with initial points $(q_0 = 6, i_0 = 0.1)$ and $(q_0 = -4, i_0 = 0.1)$ respectively, and scan down (magenta) with initial point $(q_0 = 0.3, i_0 = 0.1)$. The rest of parameters are set as in Fig. 4.

value of the normalized DC bias parameter remains the same as in Fig. 4) by considering the normalized AC amplitude as the bifurcation parameter. We always choose the value of the loss parameter within the region where an irregular pattern is observed in Fig. 4. More precisely at $\sigma = 0.15$. The bifurcation diagram and corresponding maximum Lyapunov exponent are performed once again when the normalized amplitude μ varies in the same range as in Fig. 5 (i.e., from 20 to 31.5). These graphs are shown in Fig. 6 and the results we present reveal that it features several interesting phenomena. Fig. 6(a) and 6(b) show the peak values of the normalized charge (q) and normalized current (i) inside the nonlinear SRR material as a function of the normalized amplitude μ.

Three different graphs are superimposed, plotted using three distinct initial conditions. The bifurcation branches in black and cyan are obtained by sweeping upward the normalized amplitude μ with initial points $(q_0 = 6, i_0 = 0.1)$ and $(q_0 = -4, i_0 = 0.1)$, respectively, whereas the magenta graph is obtained by sweeping downward μ with initial point $(q_0 = 0.3, i_0 = 0.1)$. As we examine each of the curves in Fig. 6(a), and 6(b), we can see that the bifurcation diagrams of the nonlinear SRR system undergoes a sequence from regular to irregular oscillation via the period-doubling scenario [38,39] as the normalized amplitude of the excitation force μ increases, starting from $\mu = 20$.

The range of μ where irregular behavior is observed is broader ($\Delta\mu \approx 5.82$) compared to the previous case [see Fig. 5(a)]. The wide range of the chaotic state is also highlighted and confirmed on the plot depicted in Fig. 6(c), where the MLE is positive over the whole range from 21.64 to 27.46. As the normalized amplitude μ of the excitation field increases, the period-doubling phenomenon occurs (which is not evident in Fig. 4), and then the motion of the charges in the material exhibits chaotic behavior once μ rises to the critical value $\mu_{c1} \approx 21.64$. When the excitation field amplitude μ is higher than μ_{c1}, this chaotic band is always observed until the critical value $\mu_{c2} \approx 27.46$. After the critical valuer μ_{c2}, the chaotic regions are eliminated, and the system flips into a periodic oscillation mode. This interesting transition is confirmed in Fig. 6(c) by a negative MLE value that appears exactly at $\mu_{c2} \approx 27.46$. The bifurcation diagrams in Fig. 6(a) and (b) show two main transitions. The first is the transition from regular mode to irregular mode (which occurs at the critical point μ_{c1}) and the second is the reverse process, i.e. the transition from irregular to regular mode occurring at the critical point μ_{c2}. One application of such a transition is the detection of a periodic signal in a noisy environment [40].

The first two critical bifurcation points for which period doubling (PD) is seen are obtained at $\mu_{p1} = 20.6$ and $\mu_{p2} = 21.5$. As an example, a series of phase trajectories illustrating the transition between regular and irregular oscillation modes of the black curve segment as μ progressively increases is shown in Fig. 7. More precisely, at $\mu = 20$, the bifurcation diagram associated with the black curve starts on period-2 signal, as presented in its frequency spectrum [Fig. 7a(i)] and the corresponding phase image [Fig. 7a(ii)]. The main peak in the spectral profile is located at the frequency $f = 0.4 f_n = f_0 = 0.4$ *THz* (where f_n is the normalized frequency), its unique subharmonic is observed at approximately half of the fundamental (i.e., at $f \approx 0.2$ *THz*) while the first high harmonic appears around 0.598 *THz* (i.e., three times greater than subharmonic frequency). Once past the first bifurcation point μ_{p1}, the system remains in the regular oscillation mode, but switches from period-2 to period-4, as shown in Fig. 7b(i) and b(ii) for $\mu = 21$. In the spectral profile [Fig. 7b(i)], one can identify the main peak at the same

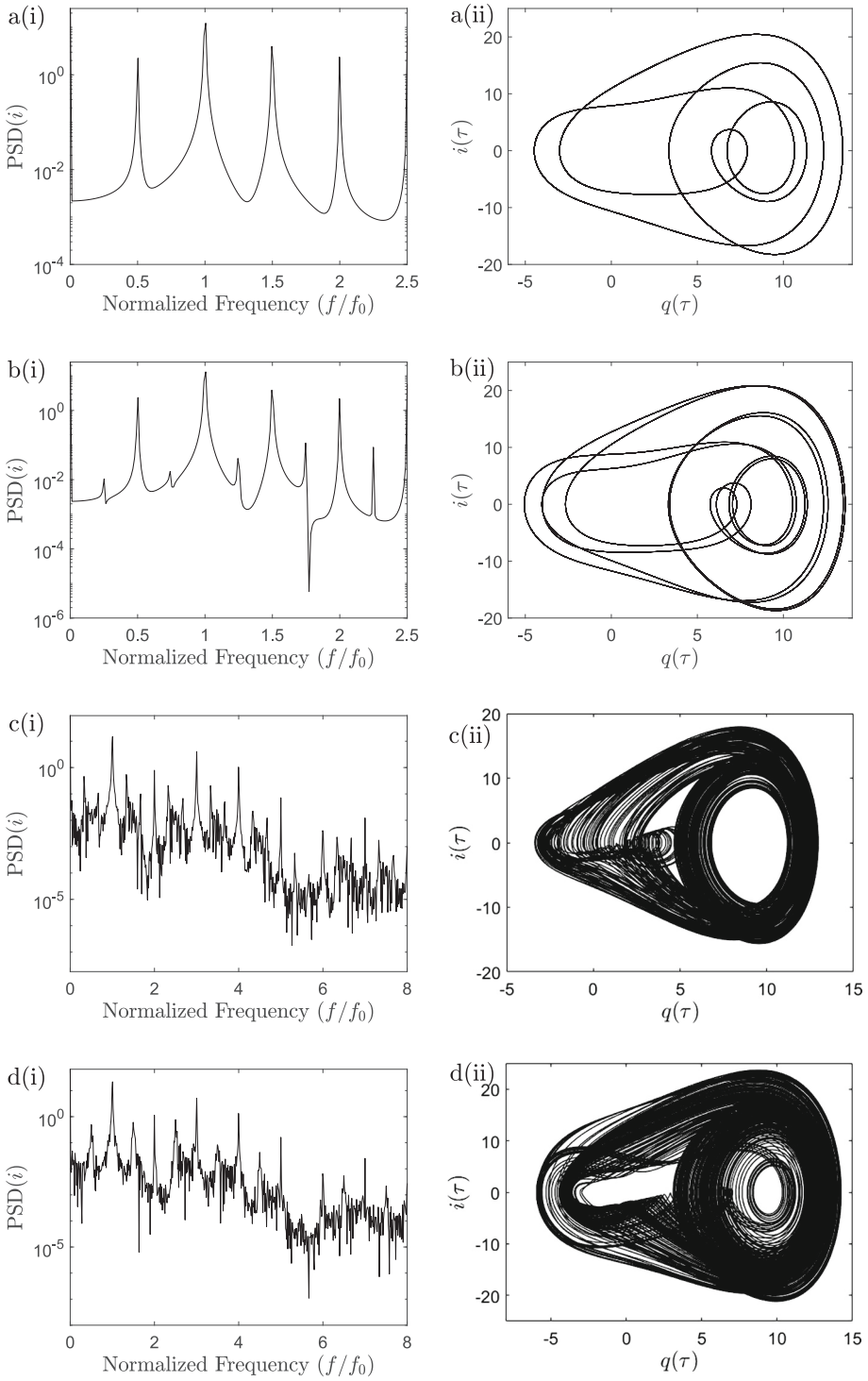

Fig. 7. Transition from a regular to an irregular regime through a period-doubling mechanism as μ increases with $\sigma = 0.15$. (a) Period-2 signal for $\mu = 20$, (b) period-4 signal for $\mu = 21$, (c) and (d) chaotic signals for $\mu = 21.8$ and $\mu = 27$, respectively. The initial point used is $(q_0 = -4i_0 = 0.1) or (q_0 = 0.3i_0 = 0.1)$ and the rest of parameters are set as in Fig. 4.

frequency as the previous oscillation mode, but with three other subharmonics peaks appearing at 0.29 *THz*, 0.2 *THz* and 0.1 *THz*, respectively, from the fundamental. The periodicity of oscillations doubles again (until chaos) when μ is slightly above the critical value μ_{p2}. As a result, chaotic signals are formed at $\mu = 21.8$ and $\mu = 27$, as shown in Fig. 7c(i) and c(ii) and Fig. 7d(i) and d(ii), respectively. The signature of chaos in these cases can be highlighted by an unlimited number of subharmonic frequencies in the power spectrum [see Fig. 7c(i) and d(i)].

Another interesting and striking region of the system to explore in Fig. 6 is the multistable domain located between $\mu = 20$ and $\mu = 21.93$. Indeed, Fig. 6 shows that below the critical value $\mu_{c3} \approx 20.77$, the three bifurcation branches (black, cyan and magenta) do not merge. But, beyond this value μ_{c3}, the cyan and magenta curve segment merge completely. The resulting curve coexists with the black bifurcation branch. The merging scenario is characterized by a jump (cyan curve) observed approximately at μ_{c3}. These features exhibited by the

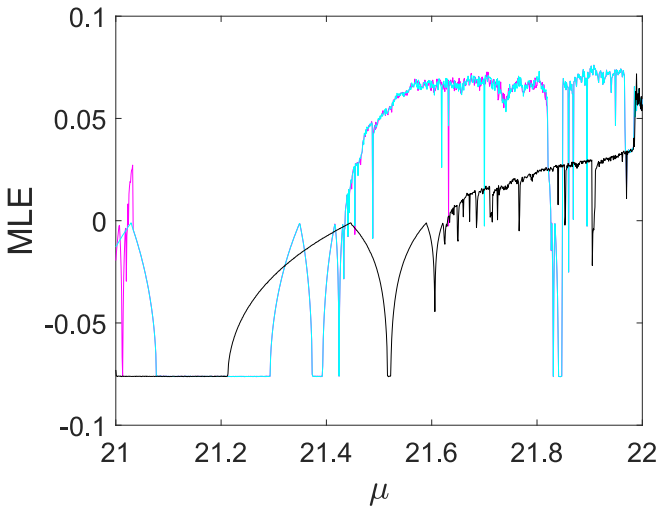

Fig. 8. Graph of the maximum Lyapunov exponent illustrating regions of coexisting dynamics and the large window where two different chaotic signals coexist. It is obtained by increasing μ from 21 to 22 with initial points $(q_0 = 6, i_0 = 0.1)$ for the cyan curve, $(q_0 = -7, i_0 = 0.1)$ for the magenta curve, and $(q_0 = -4, i_0 = 0.1)$ for the black branch. The rest of the parameters are fixed as in Fig. 6. (For interpretation of the references to color in this figure legend, the reader is referred to the web version of this article.)

bifurcation diagrams confirm the differences seen previously in two-parameter space diagrams of Fig. 4, in the same parameters range, and therefore demonstrated the coexistence of multiple stable signals [41–43] in the nonlinear SRR model. Further investigation using the coexisting graphs of the MLE allows to find an interesting and rare region with two different positive maximum Lyapunov exponents, obtained with two different pairs (q_0, i_0) of initial values. The region can be seen in the graph shown in Fig. 8, more precisely in the range from $\mu \approx 21.45$ to $\mu \approx 22$. Although this range is mostly dominated by irregular oscillations, we also observe some small windows of regular oscillations. The presence of these two positive maximum Lyapunov exponents (e.g., $\lambda_{max1} \approx 0.062$ and $\lambda_{max2} \approx 0.018$) confirms that our model is capable of generating two distinct chaotic signals for the same set of parameters. This property is particularly important for many applications [44–47]. For instance, in cryptography, the coexistence of two chaotic signals can increase the security of the secret key space. In other words, using one of the signals as an additional key in case of an attack improves the security of the encrypted image [48–50].

To highlight the different coexisting stable states in the nonlinear SRR system under EM excitation, we have developed time series, frequency spectra, phase image or cross-section of the basins of attraction by choosing the normalized amplitude of the excitation field within the multistable region of Fig. 6 and the enlarged curve investigated in Fig. 8. Fig. 9 reveals the case where up to three stable periodic states coexist. They have been obtained for $\mu = 20.5$. These periodic signals, consisting of one period-2 [Fig. 9(a), middle] and two periods-1 [Fig. 9(a), upper and lower], are represented by the time series and corresponding phase image shown in Fig. 9(a) and (b), respectively.

We have also demonstrated the coexistence of two distinct irregular signals in the system, as indicated by the basin of attraction in Fig. 10(a) (or its zoomed version in 10(b)). It was obtained for $\mu = 21.75$. In this basin, the two irregular signals are located in the black and cyan areas, respectively, and can be obtained by selecting the pair of initial value (q_0, i_0) in each of these demarcated regions. The waveforms and phase images of the associated coexisting signals are shown in Fig. 10(c) and (d) (upper and lower), respectively, where differences can be seen on both their shapes and amplitudes. Likewise, the black state corresponds to λ_{max1}, while the cyan state corresponds to λ_{max2}. It is worth mentioning here that cases of multistability involving the coexistence of three

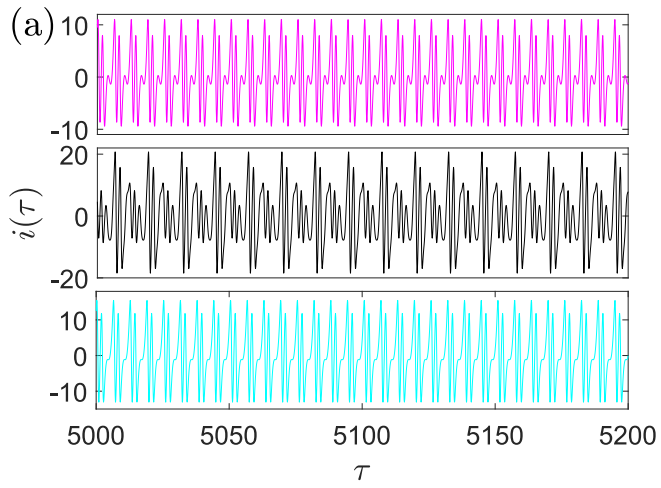

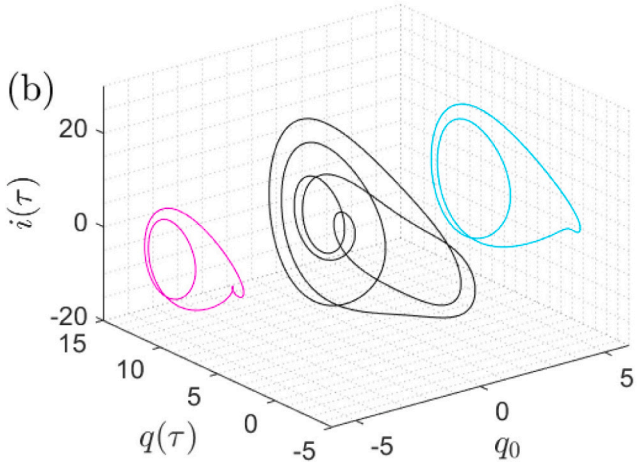

Fig. 9. Dynamics of the nonlinear SRR material showing the coexistence of three different periodic signals (two periods-1 and one period-2) for $\sigma = 0.15$ and $\mu = 20.5$. (a) Profile corresponding to the normalized temporal currents of each coexisting signal and corresponding (b) phase image of these signals. Other parameters remain the same as in Fig. 4, and the three initial points used to generate these signals are: $(q_0 = -7, i_0 = 0.1)$ for magenta, $(q_0 = -4, i_0 = 0.1)$ for black and $(q_0 = 6, i_0 = 0.1)$ for cyan. (For interpretation of the references to color in this figure legend, the reader is referred to the web version of this article.)

coexisting periodic signals (case Fig. 9) as well as two different irregular stable signals (case Fig. 10) are unique and have not been previously reported in the nonlinear SRR material [24,25].

3.5. Dynamic characteristic with bias parameter

This part is devoted to the investigation of the dynamic properties of the nonlinear model as a function of the bias parameter δ. The different oscillation regimes of the system are shown in Fig. 11 for $\mu = 35$. These bifurcation diagrams represent the local maxima of the normalized charge as δ varies from 20 to 31. It is calculated by sweeping up the control parameter δ in the corresponding interval with initial value $(q_0 = 0.3, i_0 = 0.1)$. Fig. 11(a)-(c) is obtained for $\sigma = 0.15$, $\sigma = 0.2$, and $\sigma = 0.3$, respectively. These graphs exhibit different dynamics when σ is slightly changed. In Fig. 11a(i) and c(i), chaotic regions dominate. They are delocalized and separated by small periodic windows. In these cases [Fig. 11a(i) and c(i)], irregular oscillations occur via the traditional PD mechanism as the bias parameter increases. However, Fig. 11c(i) shows bifurcation jumps, more precisely at $\delta \approx 24.1$, $\delta \approx 27$, and $\delta \approx 29.3$.

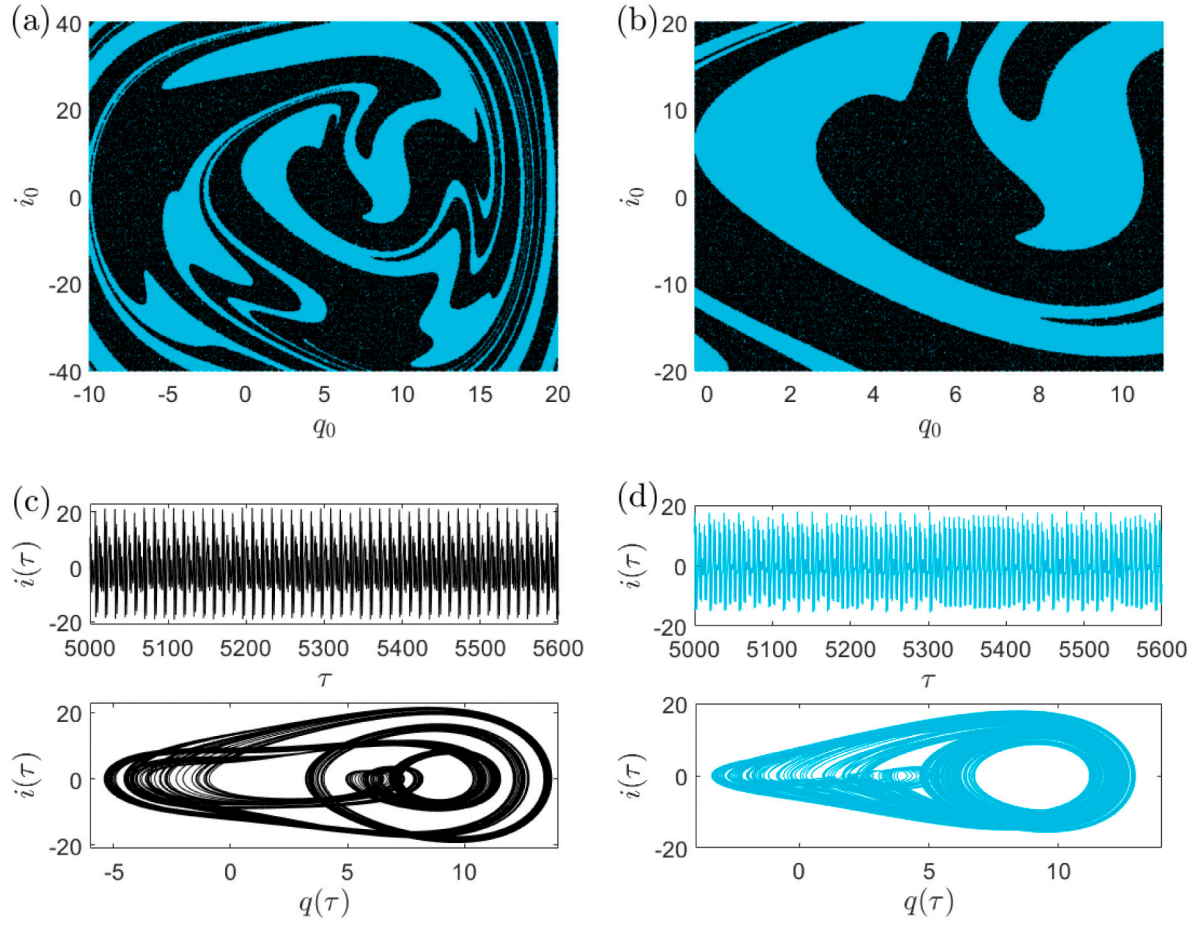

Fig. 10. (a) Cross-section of the basin of attraction and (b) it enlarged version giving initial points q_0 and i_0 when two distinct irregular signals coexist for $\sigma = 0.15$ and $\mu = 21.75$. (c)-(d) Time series (upper) and corresponding phase images (lower) of associated coexisting signals. Other parameters remain the same as in Fig. 4, and the two initial points used to generate these signals are: $(q_0 = -4, i_0 = 0.1)$ for black and $(q_0 = 6, i_0 = 0.1)$ for cyan. (For interpretation of the references to color in this figure legend, the reader is referred to the web version of this article.)

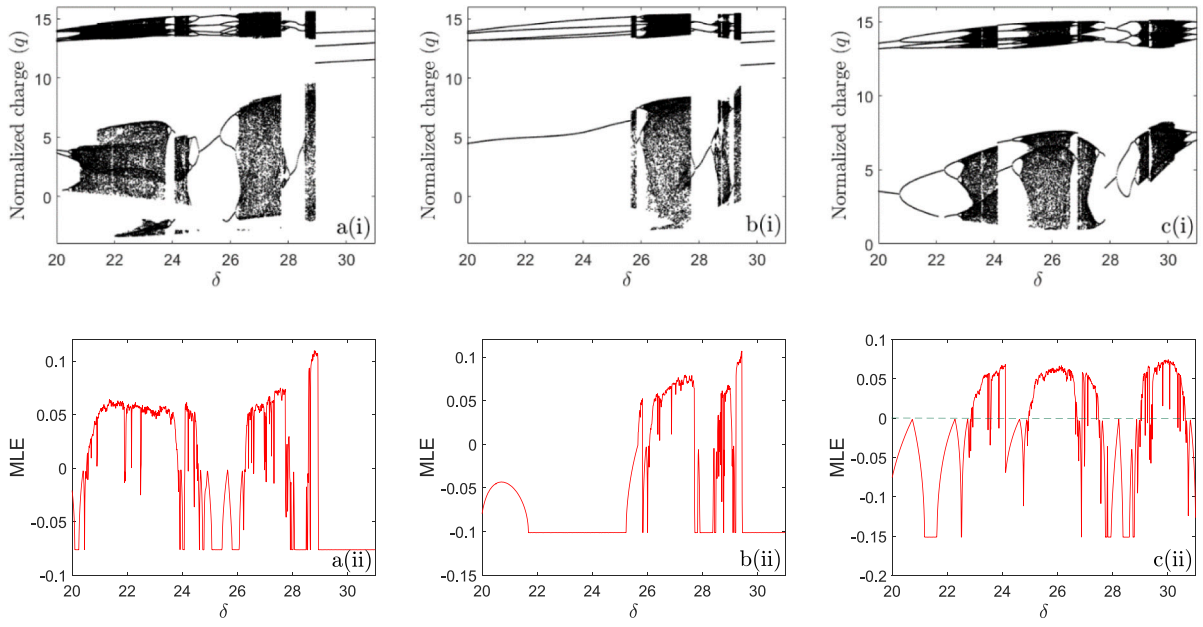

Fig. 11. Bifurcation diagrams (top) showing the dynamics of the normalized charge (q) as a function of the bias parameter δ and the corresponding MLE (bottom) plotted for $\mu = 35$, $\omega = 1.0$, $\beta = 0.4$, $\eta = 0.08$ and initial value $(q_0 = 0.3, i_0 = 0.1)$: a(i)-a(ii) $\sigma = 0.15$, b(i)-b(ii) $\sigma = 0.2$, and c(i)-c(ii) $\sigma = 0.3$.

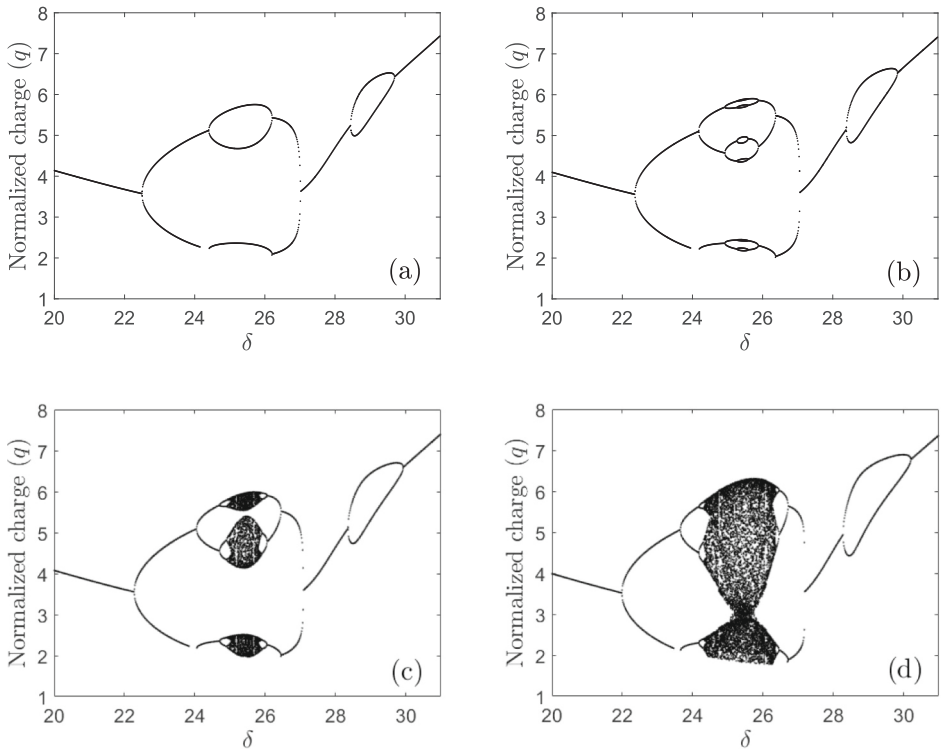

Fig. 12. Bifurcation transition scenario leading to chaotic island: (a) $\sigma = 0.37$, (b) $\sigma = 0.365$, (c) $\sigma = 0.362$, and (d) $\sigma = 0.351$. The initial values and other parameters are the same as in Fig. 11.

These jumps may be due to the presence of hysteresis or shadow branches, which can only be tracked by using different initial values (see Fig. 13). For the case shown in Fig. 11b(i), it can be observed that the periodic oscillation is dominant, while an irregular oscillation occurs in a weak band. More clearly, after a broad periodic oscillation is seen from $\delta = 20$ to $\delta_{c1} \approx 25.7$, a chaotic behavior abruptly appears above the critical δ_{c1}. For each of the curves shown in Fig. 11 (top panel), the corresponding maximum Lyapunov exponent (MLE) is shown in Fig. 11a (ii)-c(ii), confirming the different modes of oscillation observed in the bifurcation curves. The two oscillation modes are distinguished by the MLE, which is negative for a periodic mode and positive for a chaotic mode. To effectively confirm the appearance of irregular oscillations via the period-doubling mechanism, we always consider the same parameters as those fixed in Fig. 11 and the same control parameter range (i.e., $20 \leq \delta \leq 31$). The bifurcation diagram of the peak of the normalized charge within the gap is plotted for different values of σ, as shown in Fig. 12. In particular, at $\sigma = 0.37$ and $\sigma = 0.365$ [Fig. 12(a) and (b)], the two different types of PD and inverse PD are created. As can be seen in Fig. 12, at each bifurcation point, a new branch is added to the old one to form a new bifurcation of period $p = 2n$. Thus, if a period-2 bubble is created, the branch evolves into period-4 bubbles, period-8 bubbles, and so on. When the highest periodicity in the considered variation range is reached, the opposite scenario begins to occur (i.e., inverse PD). The process is repeated until the chaotic bubble is formed as shown in Fig. 12 (c) and (d) for $\sigma = 0.362$ and $\sigma = 0.351$.This exciting transition investigated here is interesting since reversals may be a way to control, perhaps even prevent, the onset of chaos in the system [51].

The coexistence of different kinds of stable signals is also highlighted when the bias constant varies. Since the trajectories followed by each competing solution in the multistable system depend on the choice of initial values, we first used the bifurcation diagrams to follow the path of coexisting states. Fig. 13 shows the coexisting bifurcation diagrams of the system computed in one of the regions where the jump phenomenon is observed in Fig. 11(c). To obtain these coexisting diagrams, we fixed $\sigma = 0.3$, $\mu = 35$ and used the continuation technique to follow the stable state with two initial values. More simply, the graph in red is calculated by increasing the value of the bias parameter, starting from the lowest value, $\delta = 29.3$, up to the highest value of the same parameter $\delta = 29.5$ with initial value $(q_0 = 2, i_0 = 0.1)$. The same procedure is applied to obtain the green curve segment, but with initial value $(q_0 = 0.3, i_0 = 0.1)$.

For the last curve, in blue, the calculation is performed by decreasing the control parameter, starting from the highest value, $\delta = 29.5$, until reaching the minimum value of the same parameter $\delta = 29.3$, with the same initial value as for the red diagram. In Fig. 13, we can see the difference between the coexisting regions. Indeed, below the critical value $\delta_{c2} \approx 29.341$, the three bifurcation branches (red, blue, and green) coexist. This situation reflects the coexistence of a chaotic state (red) with two different periodic signals (blue and green). Then, beyond this critical value δ_{c2}, two different periodic signals can coexist, or a chaotic state can coexist with a periodic signal. It is important to note that in each of these coexisting cases, the characteristic (shape and size) of the green periodic signal does not change, which is also be confirmed by the graph shown in Fig. 13(b), where the value of the MLE associated with the green curve segment remains constant ($\lambda_{max} = -0.15$). Now, the final investigation of these multistable regions revealed in the coexisting bifurcations above consists in producing the domain of the initial values (or basins of attraction) of each of the range of coexisting behaviors, that is, the coexistence of a chaotic state with two periodic orbits, the coexistence of two periodic orbits, and the coexistence of a chaotic state with a periodic one. Furthermore, we choose, within these basins of attraction, the initial values that allow to obtain each stable state.

Here, all the parameters are fixed (i.e., $\sigma = 0.3$, $\mu = 35$), and the value of δ is chosen in the graph of Fig. 13. Fig. 14 (top panel) shows three domains of initial values, for three different values of δ. These basins of attraction are plotted in the (q_0, i_0) plane, which defines the sets of initial values. Thus, the domain shown in Fig. 14a(i) represents the basin of initial values leading to one of the three stable states, chaotic (in red), periodic (in green), and another periodic (in blue). The domain in Fig. 14b(i) shows the case of a basin of initial values leading to the

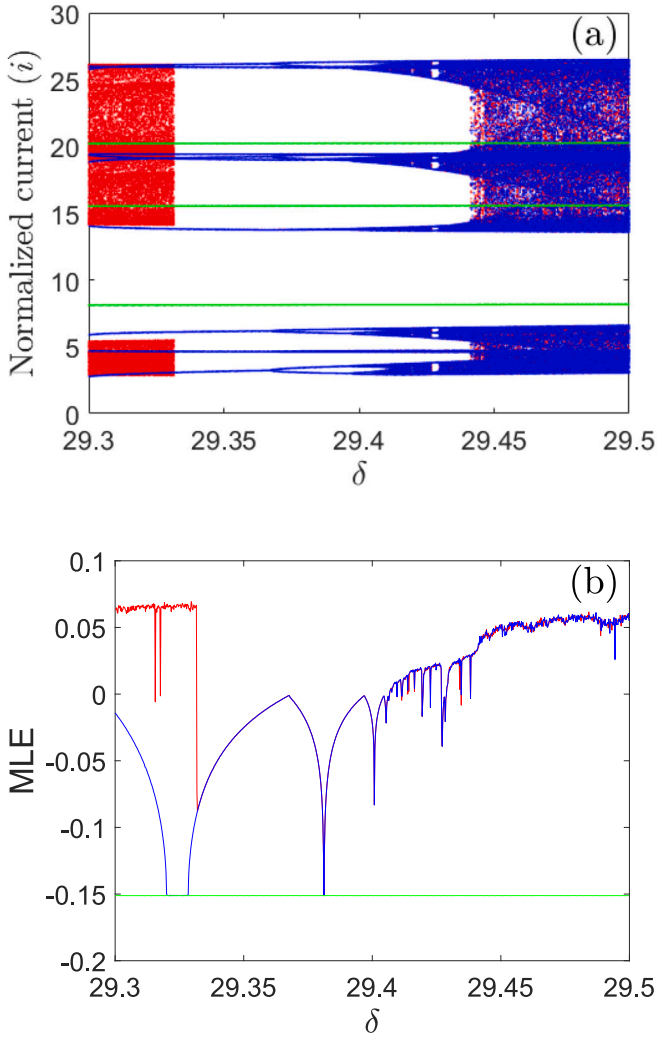

Fig. 13. Bifurcation diagrams and the corresponding graph of the maximum Lyapunov exponent showing different windows of coexisting patterns when $\sigma = 0.3$, and $\mu = 35$. The red and green branches are obtained by increasing the bias term with initial values $(q_0 = 2, i_0 = 0.1)$ and $(q_0 = 0.3, i_0 = 0.1)$, respectively, while the blue curve segment is obtained by decreasing δ with $(q_0 = 2, i_0 = 0.1)$. Other parameters remain the same as in Fig. 11. (For interpretation of the references to color in this figure legend, the reader is referred to the web version of this article.)

coexistence of two periodic signals. Finally, the basin of attraction in Fig. 14c(i) indicates initial values leading to the coexistence of a chaotic (blue) and a periodic (green) signal. The phase images and their corresponding time traces of each signal are shown in Fig. 14 (middle panel) and Fig. 14 (bottom panel), respectively. The color of each signal is the same as the color of its basin. In other words, each signal is generated by selecting the initial values in its associated basin of attraction. The results obtained in this work are comprehensive and very enriching for the understanding of the nonlinear dynamic properties of the SRR material. They show that the investigated system exhibits very complex and diverse oscillation regimes. Using various nonlinear analysis tools, we have elucidated the different mechanisms and behaviors that the system is likely to exhibit. This is an important set of results to know about a real physical system.

4. Conclusion

In this research, we have theoretically and numerically studied the nonlinear dynamics of charge carriers in a meta-atom metasurface model subjected to an DC field and illuminated by electromagnetic radiation in the terahertz frequency domain. Bi-dimensional parameter space diagrams have been used to explore the behavior of the nonlinear system and demonstrate that by controlling the normalized DC field, irregular oscillations can gradually die at high alternative fields or be born at lower alternative fields. Under different initial conditions, the results of our investigation have proved that the model exhibits both chaotic and periodic oscillation modes, and their emergence has been demonstrated in the weak alternating field condition. We found that the onset of chaos in the material results from the strong interaction between the incident wave and the cooperative charge carrier motion in the gap. When the normalized AC amplitude of the excitation field varies, the system develops a bifurcation with transition scenarios towards chaotic oscillations. The chaotic regime is located between two periodic regions, and the transition from one region to the other occurs via a period-doubling (PD) sequence or abruptly as the normalized amplitude of the field increases or decreases. Bifurcation bubbles are plotted to illustrate the PD and inverse PD mechanisms by varying the DC field parameter while controlling the loss parameter of the system.

Of most interest, the multistability phenomenon has been revealed and well-studied using coexisting graphs of Lyapunov exponent, bifurcation diagrams, phase images, time series, and basins of attraction as methods. Our results have shown a variety of coexisting stable periodic signals (with up to three periodic states) for the same set of parameters, just by varying the initial values. In addition, we have demonstrated and reported the coexistence of two separate chaotic signals under two distinct initial values in a different parameter range. To the best of the authors' knowledge, these key features of multistability have not yet been reported in this type of material and deserve to be vulgarized. Such a complicated phenomenon of multistability has been attributed to the hysteresis phenomenon found in our model when the normalized amplitude of the excitation field is increased and decreased, or to the shifting of two bifurcation points leading to the appearance of parallel branches. The direct effect of the latter is to increase the number of coexisting states in the system.

The bifurcation diagrams and MLE plots clearly illustrate how the nonlinear SRR system transitions between different dynamical regimes: from regular (periodic) to irregular (chaotic) behavior as the normalized amplitude of the external field is varied. Each bifurcation point marks a qualitative change in the response of the system, corresponding to physical transitions in the oscillation modes of the carriers within the material gap. In particular, the presence of multistable regions in the bifurcation diagrams suggests that, for certain field amplitudes, multiple stable oscillation states coexist, leading to mode switching depending on the initial conditions. This multistability and the emergence of chaos, as confirmed by positive MLE values, provide a physical explanation for the complex carrier dynamics and nonlinear phenomena observed in the SRR structure, such as enhanced field localization and hysteresis-like behavior.

Although this work successfully focuses on understanding the dynamics of the carriers, it does not explore how the electromagnetic radiation interacts with other SRR, like for metasurface. In fact, a metasurface function like an artificial brain, where information exchange is generated by the interactions between meta-atoms when exposed to electromagnetic radiation. Future research on the propagation of information patterns in a metasurface would therefore represent both an interesting application and a significant advance in the understanding of wave-matter interactions in such systems. Furthermore, since this study concerns a single unit cell, we also plan to extend this work to the collective response of a metasurface that includes the coupling between meta-atoms.

CRediT authorship contribution statement

Gervais Dolvis Leutcho: Writing – review & editing, Writing – original draft, Visualization, Validation, Supervision, Software,

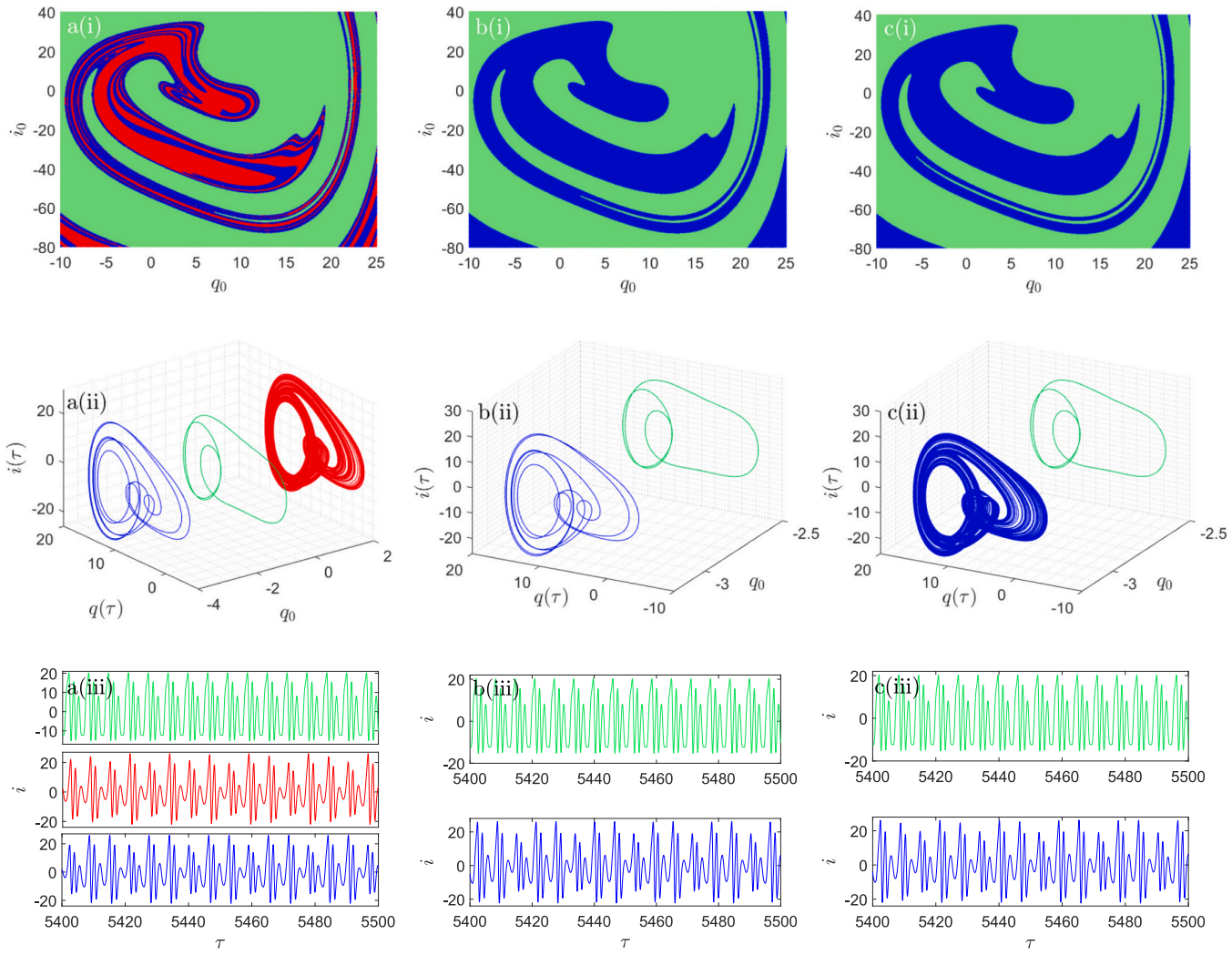

Fig. 14. Basins of attraction (top) and corresponding phase images (middle), time series (bottom) illustrating the variety of coexisting patterns in the system obtained at $\delta = 29.32$ (first column), $\delta = 29.36$ (second column), and $\delta = 29.46$ (third column). Each color of the basin of attraction corresponds to a well-defined region of the coexisting state, so its phase portrait is shown on the middle line. Other parameters remain the same as in Fig. 11.

Resources, Project administration, Methodology, Investigation, Formal analysis, Data curation, Conceptualization. **Gabriel Gandubert:** Software, Resources, Data curation. **Lyne Woodward:** Writing – review & editing, Writing – original draft, Validation, Supervision, Data curation, Funding acquisition. **François Blanchard:** Writing – review & editing, Writing – original draft, Validation, Supervision, Project administration, Funding acquisition, Conceptualization.

Declaration of competing interest

The authors declare that they have no known competing financial interests or personal relationships that could have appeared to influence the work reported in this paper.

Acknowledgment

The authors acknowledge financial support from NSERC Grant No. RGPIN-2019-05853, Grant No. RGPIN-2023-03322 and the CRC tier2 Grant No. CRC-2019-00127 on Spatiotemporal encryption of THz light.

Data availability

The data that supports the findings of this study are available from the corresponding author upon reasonable request.

References

[1] Leitenstorfer A, Moskalenko AS, Kampfrath T, Kono J, Castro-Camus E, Peng K, et al. The 2023 terahertz science and technology roadmap. J Phys D Appl Phys 2023;56:223001.
[2] Blanchard F, Chai X, Tanaka T, Arikawa T, Ozaki T, Morandotti R, et al. Terahertz microscopy assisted by semiconductor nonlinearities. Opt Lett 2018;43:4997–5000.
[3] Blanchard F, Nkeck JE, Guiramand L, Zibod S, Dolgaleva K, Arikawa T, et al. Two-dimensional space–time terahertz memory in bulk SrTiO 3. Optica 2022;9(9):980–6. https://doi.org/10.1364/OPTICA.463730.
[4] Fan K, Hwang HY, Liu M, Strikwerda AC, Sternbach A, Zhang J, et al. Nonlinear terahertz metamaterials via field-enhanced carrier dynamics in GaAs. Phys Rev Lett 2013;110:217404.
[5] Kang BJ, Rohrbach D, Brunner FD, Bagiante S, Sigg H, Feurer T. Ultrafast and low-threshold THz mode switching of two-dimensional nonlinear metamaterials. Nano Lett 2022;22:2016–22.
[6] Keiser GR, Karl N, Ul Haque SR, Brener I, Mittleman DM, Averitt RD. Structural tuning of nonlinear terahertz metamaterials using broadside coupled split ring resonators. AIP Adv 2021;11:095103.
[7] Keren-Zur S, Tal M, Fleischer S, Mittleman DM, Ellenbogen T. Generation of spatiotemporally tailored terahertz wavepackets by nonlinear metasurfaces. Nat Commun 2019;10:1778.
[8] Hirori H, Blanchard F, Tanaka K. Single-cycle terahertz pulses with amplitudes exceeding 1 MV/cm generated by optical rectification in LiNbO3. Appl Phys Lett 2011;98:091106.

[9] Guiramand L, Nkeck J, Ropagnol X, Ozaki T, Blanchard F. Near-optimal intense and powerful terahertz source by optical rectification in lithium niobate crystal. Photonics Research 2022;10:340–6.
[10] Tóth G, Polónyi G, Hebling J. Tilted pulse front pumping techniques for efficient terahertz pulse generation. Light: Science & Applications 2023;12:256.
[11] Hafez H, Chai X, Ibrahim A, Mondal S, Férachou D, Ropagnol X, et al. Intense terahertz radiation and their applications. J Opt 2016;18:093004.
[12] Howe NP, Bundell S. How 'metadevices' could make electronics faster. Nature 2023. https://doi.org/10.1038/d41586-023-00467-6.
[13] Zhang Q, Barri K, Jiao P, Lu W, Luo J, Meng W, et al. Meta-mechanotronics for self-powered computation. Mater Today 2023;65:78–89.
[14] Huang T, Zhao X, Zeng S, Crunteanu A, Shum PP, Yu N. Planar nonlinear metasurface optics and their applications. Rep Prog Phys 2020;83:126101.
[15] Emara MK, Kundu D, Macdonell K, Rufail L, Gupta S. Reconfigurable metasurface reflectors using split-ring resonators with co-designed biasing for magnitude/phase control. IEEE Trans Antennas Propag 2024;78:7425–30.
[16] Tsai WY, Chung TL, Hsiao HH, Chen JW, Lin RJ, Wu PC, et al. Second harmonic light manipulation with vertical split ring resonators. Adv Mater 2019;31:1806479.
[17] Leutcho GD, Woodward L, Blanchard F. Nonlinear dynamics of a single-gap terahertz split-ring resonator under electromagnetic radiation. Chaos 2023;33(10): 103131. https://doi.org/10.1063/5.0157489.
[18] Leutcho GD, Gandubert G, Woodward L, Blanchard F. Multistability via field-enhanced carrier dynamics in a single-gap nonlinear terahertz split-ring resonator with loss parameter control. Phys Rev E 2025;111:044209.
[19] Hossain M, Pati N, Pal S, Rana S, Pal N, Layek G. Bifurcations and multistability in a food chain model with nanoparticles. Math Comput Simul 2021;190:808–25.
[20] Pati N, Garai S, Hossain M, Layek G, Pal N. Fear induced multistability in a predator-prey model. International Journal of Bifurcation and Chaos 2021;31: 2150150.
[21] Pati N, Rech PC, Layek G. Multistability for nonlinear acoustic-gravity waves in a rotating atmosphere. Chaos 2021;31:023108.
[22] Deb P, Layek G. Controlling the period-bubbling route to Chaos. International Journal of Bifurcation and Chaos 2024;34:2450123.
[23] Layek G. An introduction to dynamical systems and chaos. Springer; 2015.
[24] Lazarides N, Molina MI, Tsironis GP, Kivshar YS. Multistability and localization in coupled nonlinear split–ring resonators. Phys Lett A 2010;374:2095–7.
[25] Shena J, Lazarides N, Hizanidis J. Multi-branched resonances, chaos through quasiperiodicity, and asymmetric states in a superconducting dimer. Chaos 2020; 30:123127.
[26] Hellen EH. Rlc resonator with diode nonlinearity: bifurcation comparison of numerical predictions and circuit measurements. Chaos 2024;34(7):073104. https://doi.org/10.1063/5.0206829.
[27] Lazarides N, Hizanidis J, Tsironis G. Controlled generation of chimera states in SQUID metasurfaces using DC flux gradients. Chaos, Solitons Fractals 2020;130: 109413.
[28] Zhang S, Wong CL, Zeng S, Bi R, Tai K, Dholakia K, et al. Metasurfaces for biomedical applications: imaging and sensing from a nanophotonics perspective. Nanophotonics 2020;10:259–93.
[29] Cocker TL, Jelic V, Gupta M, Molesky SJ, Burgess JA, Reyes GDL, et al. An ultrafast terahertz scanning tunnelling microscope. Nat Photonics 2013;7:620–5.
[30] Powell DA, Shadrivov IV, Kivshar YS, Gorkunov MV. Self-tuning mechanisms of nonlinear split-ring resonators. Appl Phys Lett 2007;91(14):144107. https://doi.org/10.1063/1.2794733.
[31] Amirkhan F, Sakata R, Takiguchi K, Arikawa T, Ozaki T, Tanaka K, et al. Characterization of thin-film optical properties by THz near-field imaging method. JOSA B Opt Phys 2019;36(9):2593–601. https://doi.org/10.1364/JOSAB.36.002593.
[32] Yu Y, Lin Y-S. Multi-functional terahertz metamaterial using symmetrical and asymmetrical electric split-ring resonator. Results in Physics 2019;13:102321.
[33] Wolf A, Swift JB, Swinney HL, Vastano JA. Determining Lyapunov exponents from a time series. Physica D: nonlinear phenomena 1985;16:285–317.
[34] Bao H, Rong K, Chen M, Zhang X, Bao B. Multistability and synchronization of discrete maps via memristive coupling. Chaos, Solitons Fractals 2023;174:113844.
[35] Nasari H, Abrishamian MS. Terahertz bistability and multistability in graphene/dielectric Fibonacci multilayer. Appl Opt 2017;56:5313–22.
[36] Njitacke ZT, Awrejcewicz J, Tsafack N, Kudra G, Kengne J. Complex dynamics, released energy, and multistability in a single-layered graphene sheet under periodic loads. Phys Scr 2023;98:085228.
[37] Valagiannopoulos C. Multistability in coupled nonlinear metasurfaces. IEEE Trans Antennas Propag 2022;70:5534–40.
[38] Rajagopal K, Jafari S, Li C, Karthikeyan A, Duraisamy P. Suppressing spiral waves in a lattice array of coupled neurons using delayed asymmetric synapse coupling. Chaos, Solitons Fractals 2021;146:110855.
[39] Venkatesh J, Karthikeyan A, Chedjou JC, Jacques K, Karthikeyan R. Coupling induced dynamics in a chain-network of four two-well duffing oscillators: theoretical analysis and microcontroller-based experiments. Journal of Vibration Engineering & Technologies 2024;12:8815–28.
[40] Shen L, Xia J, Ezawa M, Tretiakov OA, Zhao G, Zhou Y. Signal detection based on the chaotic motion of an antiferromagnetic domain wall. Appl Phys Lett 2021;118: 012402.
[41] Kengne LK, Signing VRF, Sebastiano DR, Tekam RBW, Tegnitsap JVN, Zhao M, et al. Simplest transistor-based chaotic circuit with extreme events: statistical characterization, synchronization, and analogy with interictal spikes. Chaos, Solitons Fractals 2025;191:115894. https://doi.org/10.1016/j.chaos.2024.115894.
[42] Sriram S, Kemgang Kana L, Rakhmatullaeva M, Rajagopal K, Kengne J. Multistability and four-scroll chaos in a pair of coupled second-order damped oscillators with hyperbolic sine function: theoretical study and circuit simulation. Circuits Syst Signal Process 2024;43:2016–50.
[43] Zhang S, Li Y, Lu D, Gao X, Li C, Chen G. A novel memristor regulation method for chaos enhancement in unidirectional ring neural networks. IEEE Trans Circuits Syst I Regul Pap 2025:1–9. 3536028.
[44] Tegnitsap JVN, Njitacke ZT, Barà C, Fozin TF, Fotsin HB, Valdes-Sosa PA, et al. A van der pol-like complementary chaotic oscillator: design, physical realizations, dynamics, and physiological data augmentation prospect. Chaos, Solitons Fractals 2025;191:115886. https://doi.org/10.1016/j.chaos.2024.115886.
[45] Telem ANK, Fonzin TF, Sone ME, Tabekoueng ZN, Fotsin HB. A chaos-based DS-CDMA transmission and synchronization for multi-leads medical ECG/EEG through AWGN and Rayleigh Channels. Multimed Tools Appl 2024;83:425–48.
[46] Zhang S, Chen C, Zhang Y, Cai J, Wang X, Zeng Z. Multidirectional multidouble-scroll hopfield neural network with application to image encryption. IEEE Trans Syst Man Cybern Syst 2024;55:735–46.
[47] Zhang S, Peng X, Wang X, Chen C, Zeng Z. A novel memristive multiscroll multistable neural network with application to secure medical image communication. IEEE Trans Circuits Syst Video Technol 2024;35:1774–86.
[48] Lai Q, Yang L, Hu G, Guan Z-H, Iu HH-C. Constructing multiscroll memristive neural network with local activity memristor and application in image encryption. IEEE Trans Cybern 2024;54:4039–48.
[49] Leutcho GD, Wang H, Fozin TF, Sun K, Njitacke ZT, Kengne J. Dynamics of a new multistable 4D hyperchaotic Lorenz system and its applications. Int J Bifurc Chaos 2022;32:2250001.
[50] Li B, Sun K, Wang H, Liu W. A delay-disturbance method to counteract the dynamical degradation of digital chaotic systems and its application. Chaos, Solitons Fractals 2024;182:114843.
[51] Stone L. Period-doubling reversals and chaos in simple ecological models. Nature Publishing Group UK London; 1993.